In Situ Localized Surface Plasmon Resonance (LSPR) Spectroscopy to Investigate Kinetics of Chemical Bath Deposition of CdS Thin Films

ARTICLE *in* THE JOURNAL OF PHYSICAL CHEMISTRY C · FEBRUARY 2015

Impact Factor: 4.77 · DOI: 10.1021/jp512738b

THE JOURNAL OF PHYSICAL CHEMISTRY C

Article

pubs.acs.org/JPCC

In Situ Localized Surface Plasmon Resonance (LSPR) Spectroscopy to Investigate Kinetics of Chemical Bath Deposition of CdS Thin Films

Humaira Taz,[†] Rose Ruther,[‡] Abhinav Malasi,[§] Sagar Yadavali,[§] Connor Carr,[∥] Jagjit Nanda,*[,†,‡,§] and Ramki Kalyanaraman*[,†,§,∥]

[†]Bredesen Center, The University of Tennessee Knoxville, Knoxville, Tennessee 37996, United States

[‡]Materials Science and Technology Division, Oak Ridge National Laboratory, Oak Ridge, Tennessee 37831, United States

[§]Department of Chemical and Biomolecular Engineering, The University of Tennessee Knoxville, Knoxville, Tennessee 37996, United States

[∥]Department of Materials Science and Engineering, The University of Tennessee Knoxville, Knoxville, Tennessee 37916, United States

ABSTRACT: Techniques that can characterize the early stages of thin film deposition from liquid phase processes can aid greatly in our understanding of mechanistic aspects of chemical bath deposition (CBD). Here we have used localized surface plasmon resonance (LSPR) spectroscopy to monitor the in situ kinetics of early stage growth of cadmium sulfide (CdS) thin films on Ag nanoparticle on quartz substrates. Real-time shift during CdS deposition showed that the LSPR wavelength red-shifted rapidly due to random deposition of CdS on the substrate but saturated at longer times. LSPR modeling showed that these features could be interpreted as an initial deposition of CdS islands followed by preferential deposition onto itself. The CdS also showed significantly enhanced Raman signals up to 170 times due to surface-enhanced Raman scattering (SERS) from the CdS/Ag NP regions. The ex situ SERS effect supported the LSPR shift, suggesting that these techniques could be used to understand nucleation and growth phenomena from the liquid phase.

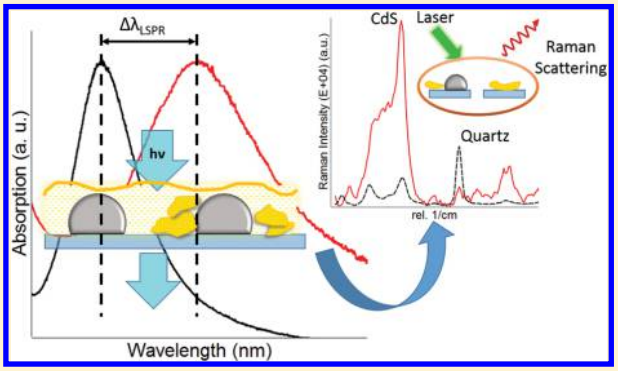

INTRODUCTION

Over the last few decades liquid phase chemical bath deposition (CBD) has become an important technique to deposit metal, semiconductor, and dielectric thin films over large areas due to its low cost and scalability. It has been used for photovoltaic devices,[1−5] infrared hollow wave guides,[6] magnetic semiconductor devices,[7] supercapacitors,[8] photocatalysis,[9] optoelectronic devices,[10] cholesterol sensing,[11] and to manufacture nanoparticles.[12] However, understanding the CBD process has primarily been through a postdeposition analysis of film microstructure resulting from varying reaction parameters, such as temperature, solution concentration, pH, and fluid flow.[2−5,13] Recently, a small number of studies have appeared in which real time investigations have been used, all with the goal of better understanding the nucleation and growth process of CBD film deposition. These include techniques based on quartz crystal microbalance measurement,[4] turbidity measurements,[14] and optical reflectance measurement.[15] The existing in situ studies[4,14,15] revealed three regimes of film growth: first, nucleation on the substrate surface; second, a linear growth rate resulting in a compact layer; and third, a cluster mechanism that created a porous layer. However, these studies were performed under dip-coating conditions where there is a higher possibility that the CdS particles precipitate in the solution and then stick to the substrate, hence contributing to the final microstructure. On the other hand, for deposition under dynamic flow deposition conditions, not only can the growth rate be quite different from dip coating but also some of the underlying mechanisms of growth could be different. Recently, the dynamic deposition process has been investigated by Greil et al.[16] and Jang et al.[17] By using in situ soft X-ray absorption spectroscopy (XAS) Greil et al. were able to identify real-time Zn complexes during the CBD process.[16] Jang et al. studied electroless deposition of gold film by flowing the solution over the substrate and demonstrated that in situ photoluminescence and surface plasmon measurements could reveal important aspects of the deposition process.[17]

Here, we propose a spectroscopic technique based on measuring changes to the localized surface plasmon resonance (LSPR) that can capture the kinetics occurring within nanoscale volumes of the fluid phase, potentially leading to very accurate information on early stage growth kinetics. LSPR is well-established as a technique to sense refractive index changes with extremely high, molecular-level sensitivity, leading

Received: December 21, 2014
Revised: February 10, 2015
Published: February 11, 2015

DOI: 10.1021/jp512738b
J. Phys. Chem. C 2015, 119, 5033−5039

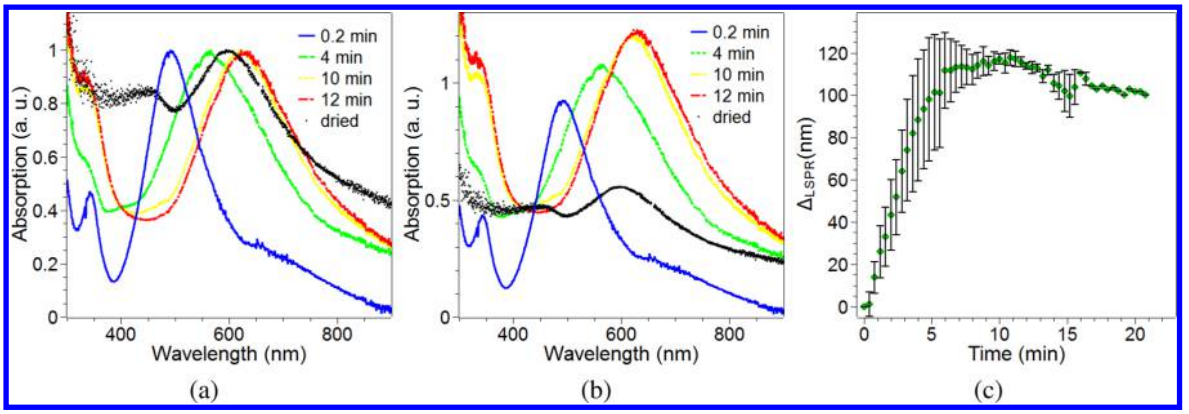

Figure 1. (a) Intensity normalized in situ absorption spectra showing shift in the LSPR spectral peak position over 12 min of CdS deposition. The 0.2 min corresponds to the peak position immediately following the flow of the CBD solution over the Ag NP/quartz substrate. (b) In situ absorption spectra for CdS deposition onto the Ag NP/quartz substrate taken at various times. The dried sample corresponds to the ex situ measurement following deposition for 12 min and drying of the sample. (c) Plot of in situ shift $\Delta\lambda_{LSPR}$ as a function of CdS deposition time.

to applications in fields such as biomedicine.[18−23] The principle is that the spectral position of the LSPR absorption peak of a plasmonic metal nanoparticle (NP) changes based on the dielectric constant of the surrounding environment. On the basis of electromagnetic field calculations around a plasmonic NP, Willets and Van Duyne quantified the shift in the wavelength position of the LSPR peak when an adsorbate molecule is attached to it.[19] In their model, the shift is related to the change in the refractive index Δn, as $\Delta_{max} = m\Delta n\,[1 - \exp(-2d/l_d)]$, where m is the bulk refractive index sensitivity of the nanoparticles, Δn the change in the refractive index induced by the adsorbate; d the effective adsorbate layer thickness, and l_d the characteristic EM field decay length.[19] We used Ag nanoparticles (NPs) that exhibit strong LSPR peaks as the nanoscale sensor to detect early stages of CdS film deposition and growth. CdS was chosen due to the diverse applications resulting from its semiconducting, dielectric, and optical behaviors in thin film and/or nanoparticle form.[3,6,24,25] The substrate was held in a transparent flow cell, and in situ measurements of the transmission spectra were obtained to monitor the dynamic CdS film growth in real-time. By correlating these in situ studies with ex situ studies of the time-dependent morphology and chemical distribution on the surface using scanning electron microscopy, atomic force microscopy, and Raman spectroscopy, a good understanding of the LSPR shift in the context of film deposition was achieved.

RESULTS AND DISCUSSION

Figure 1a shows the typical time-dependent optical absorption spectra over 12 min of the flow of the CdS solution over the Ag NP/quartz substrate. These spectra were obtained from the in situ transmission spectra by using the transformation: absorption = log (100/transmission), and the absorption values were then normalized with respect to the value where the plasmon peak occurs. The large absorption peak at 490 nm for the sample labeled as 0.2 min (min) corresponds to the LSPR peak for the Ag NP/quartz system measured as soon as the CdS flow was started. A dynamic change in the absorbance curve was evident for the longer time measurements (curves labeled 4, 10, and 12 min), and this was due to the deposition of CdS (which has a refractive index of $n = 2.5$[26]) on the Ag NP/quartz substrate. Besides a red shift in the LSPR, a significant change in absorption could also be seen in the wavelength range of ∼350−500 nm, as evident from Figure 1b, which shows the raw absorption spectra for the dynamic deposition run shown in Figure 1a. Unlike in the normalized spectra, there is a significant decrease in absorption by the sample under the dynamic situation (12 min) versus the dried case (after 12 min of deposition). This is because of the large volume of fluid present in the dynamic case, which absorbs light, thus decreasing the sensitivity to measuring changes. In addition, since the fluid volume can change slightly during the flow in the open cell used in our measurements, the absolute value of the absorption peak could not be used as a reliable measure of the CdS deposition.

In Figure 1c, the experimentally measured in situ LSPR shift (green ◆), averaged over multiple measurements, is shown with respect to deposition time. The LSPR shift was calculated with respect to the 0.2 min time substrate. The uncertainty bars corresponded to 1 standard deviation from the mean. This LSPR shift showed three distinct behaviors. For early times, it was found to increase rapidly (0.2 to 5 min), subsequently the shift slowed and appeared to saturate (5 to 12 min), and finally, a small drop in shift was observed for times beyond 12 min. Next, we measured the average film height deposited by using the AFM technique to scan across steps in the deposited and dried film, as shown in Figure 2a. The average film height measured by this approach is shown in Figure 2b for deposition onto Ag NP/quartz (●) and quartz (□). From this, we found that the film height for the largest LSPR shift, which occurred in the saturation regime at a time of 12 min was 19.4 ± 5.5 nm. The SEM image in the inset shows that an open fibril network morphology occurs for the CdS film on quartz and is compared later in the paper with the SEM images of CdS grown on the Ag NP/quartz substrate.

In order to interpret our experimental observations, we utilized an LSPR sensing model, keeping in mind that the deposition of CdS onto the underlying plasmonically sensitive Ag NPs can occur either as a uniform two-dimensional (2D) coating or as discrete three-dimensional (3D) islands, as depicted in Figure 3a. Moreover, keeping in mind that the Ag NPs have an LSPR-sensitive zone surrounding them (as depicted in Figure 3a), 2D versus 3D deposition of CdS within this zone can lead to significant differences in the maximum LSPR shift at saturation. To estimate this saturation LSPR shift, we utilized an effective medium approach (EMA) to calculate the effective relative dielectric permittivity for the case when

DOI: 10.1021/jp512738b
J. Phys. Chem. C 2015, 119, 5033−5039

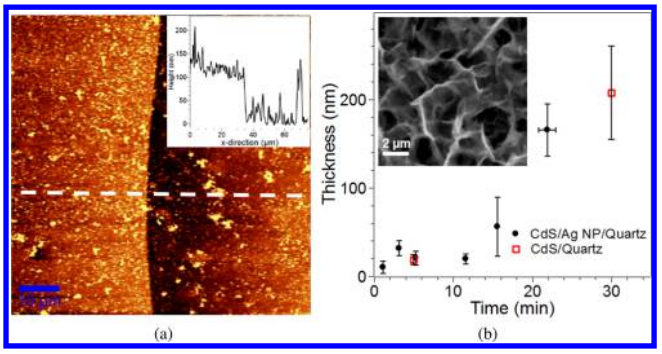

Figure 2. (a) A typical AFM scan across the film step in the 15 min deposition onto Ag NP/quartz. (inset) A line scan across the film step is shown, from which the effective deposited film height was determined. (b) Plot of the effective film height as a function of deposition time obtained from AFM scans. ● corresponds to measurements on the Ag NP/quartz, while □ corresponds to the quartz substrate. The inset shows the SEM image of the morphology of CdS film deposited on bare quartz substrate for ∼30 min.

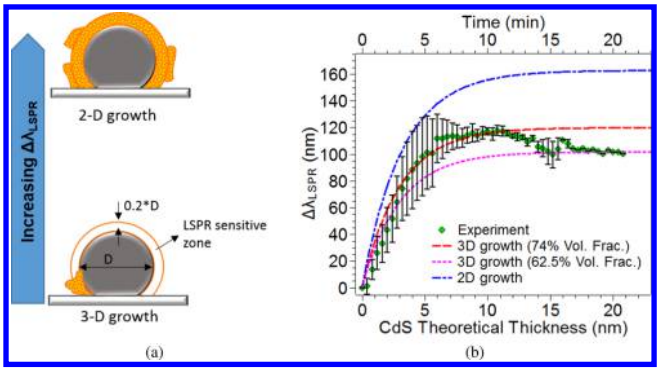

Figure 3. (a) Schematic illustration of the nanoparticle, the LSPR sensitive zone, the two extreme types of deposition (i.e., two- or three-dimensional) that can occur, and trend in LSPR shift corresponding to the two deposition types. (b) Comparison of experimental data (symbols) to the model prediction of LSPR shift for the various deposition types (lines).

CdS replaces the surrounding medium (solution) of the Ag NP/quartz substrate using a binary mixing model described in refs 27 and 28. For a two component system, the effective permittivity can be expressed as

$$\epsilon_{\text{eff}}(\gamma) = \left[\frac{f_a}{\epsilon_A} + \frac{f_h}{\epsilon_h} - \frac{2f_a f_h(\epsilon_a - \epsilon_h)^2}{3\epsilon_a\epsilon_h[\epsilon_h\gamma + \epsilon_a(1-\gamma)]}\right]^{-1} \quad (1)$$

where f_a and f_h are the volume fractions of the two constituent materials with permittivity ϵ_a and ϵ_h, respectively, and $\gamma = 1 - 2f_a/3$, which corresponds to the exact Maxwell-Garnet EMA mixing rule. In our case, f_a was the volume fraction of CdS and f_h was that of solution. From this calculation, we obtained the effective refractive index n_{eff} from $1/2\{[Re(\epsilon_{\text{eff}}^2) + \text{Im}(\epsilon_{\text{eff}}^2)]^{1/2} + Re(\epsilon_{\text{eff}})\}^{1/2}$, which was then used to estimate the theoretical shift as $\Delta\lambda_{\text{Th}} = m(n_{\text{eff}} - n_{\text{liquid}})[1 - \exp(-2d/l_d)]$. To model uniform 2D deposition, the value of f_a was set at 1.0, which meant that 100% of the Ag NP was uniformly coated with CdS of thickness d. For the relevant dielectric permittivities (in the visible wavelength spectrum) of the various materials, we used $\epsilon = (2.5 + 0.23\text{i})^2$ for CdS, where the real refractive index $n = 2.5$ and imaginary part of refractive index $\kappa = 0.23$ were from ref 26. Noting that the solution was 99.7% (by volume) water, we used the dielectric of water of $\epsilon = 1.77$. For the sensitivity factor m, we used the literature value for spherical Ag particles of 138 nm/RIU (RIU = refractive index units).[29] The result of the calculations for the 2D deposition is shown in Figure 3b (dashed blue line). From this it is immediately apparent that 2D growth cannot be occurring since the predicted shift in LSPR was significantly larger than the experimental values for all times, including in the saturation regime. We should point out that the 2D model here is identical to applying the Willets and Van Duyne expression since that is also based on a uniform change in refractive index around the particle (i.e., $n_{\text{CdS}} - n_{\text{liquid}}$). In order to model 3D growth, f_a had a value < 1, implying that only a fraction (f_a) of the Ag NP was covered with a CdS layer of thickness d. This value of f_a was used as a free fitting parameter, and the best fit to the experimental LSPR saturation was obtained for a value of 74%. This result is shown in Figure 3b (dashed red line), and clearly, a better match to the experiment is evident over the 2D case. It should be emphasized that since the fraction f_a can change with deposition time, using a single value for the entire fit may not be physically realistic. Nevertheless, the good match to the

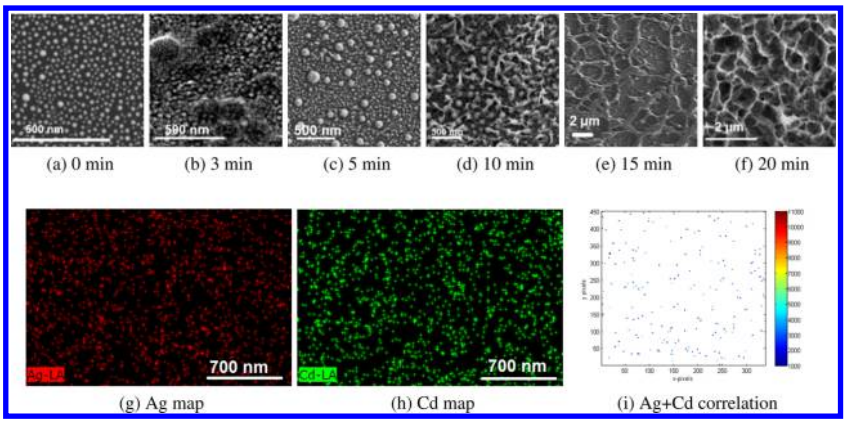

Figure 4. Results of SEM morphology and EDS mapping. (a–f) show SEM images of the morphology of CdS corresponding to 0, 3, 5, 10, 15, and 20 min, respectively. (Note the different scale bars for the (e) 15 and (f) 20 minute cases.) (g) EDS map of Ag in the 5 min sample. (h) EDS map of Cd in the 5 min sample. (i) A correlation map of the Ag+Cd generated from (g and h) plots of overlapping regions of Ag and Cd. Very small correlation was seen between the position of the Ag and the depositing CdS. The pixel size for each of the x and y dimension corresponded to 5.4 nm.

DOI: 10.1021/jp512738b
J. Phys. Chem. C 2015, 119, 5033−5039

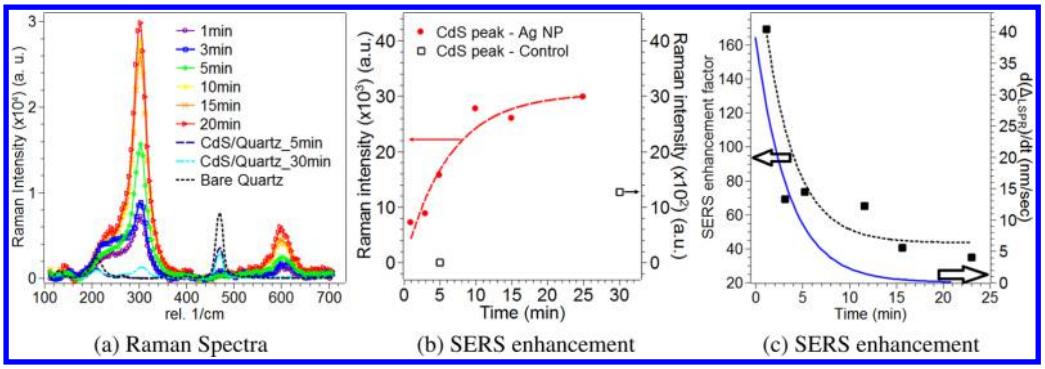

Figure 5. (a) Raman spectra of CdS/Ag NP/quartz and CdS/quartz samples for various CdS deposition times. (b) The change in the integrated intensity of the primary CdS peak at 305 nm^{-1} with deposition time; the plot for CdS/Ag NP/quartz corresponds to the left y axis and that for CdS/quartz corresponds to the right y axis. (c) Plot of the calculated SERS enhancement factor (■; left axis). The dashed line is an exponential decay function as a guide to the eye. The time rate of change of the experimentally measured Δ_{LSPR} (blue curve, right axis) as a function of CdS deposition time.

experimental curve suggests that the deposition is clearly 3D in nature. To verify if our model prediction is consistent with the deposition morphology of the CdS, we performed SEM investigations, as discussed next.

Figure 4 (panels a–f) shows the SEM morphology following dynamic deposition for 0, 3, 5, 10, 15, and 20 min, respectively. The 0 min image simply shows the Ag NP/quartz system before any CdS has been deposited on it. The 3 and 5 min images show CdS growth in the form of localized islands which appear to be randomly distributed with respect to the underlying Ag NP structure. This implied that the Ag NPs did not strongly influence the deposition of the CdS. In the 10 min case, the early stages of a branching network of CdS was seen to start forming, with the underlying Ag NP structure clearly still evident. After 15 min, the morphology showed a well-defined open fibril network with continued evidence for the underlying Ag NPs. For the 20 min case, only a fibril network or a porous CdS film was visible.

The SEM results for the early times, up to 5 min, clearly supported the model interpretation of a 3D deposition of CdS. Here, the CdS was being deposited as random islands onto the underlying Ag NP/quartz system. Second, the saturation in the LSPR signal predicted by the 3D model (74% coverage) intrinsically implied that CdS was preferentially being deposited onto itself, as opposed to onto the still-available Ag LSPR-sensitive regions. This feature is also evident from the SEM for the later times (i.e., 10 to 15 min), which show that despite the underlying Ag NP/substrate system being clearly available, the LSPR has saturated. Thus, the experimentally observed saturation can be explained as a preferential deposition of CdS on itself, clearly supporting the LSPR model prediction of 3D deposition.

One remaining feature to explain in the experimental LSPR shift was the decrease in shift occurring after 12 min. On the basis of the model, the decrease in LSPR shift for times greater than 12 min can occur when the effective refractive index n_{eff} decreases. Therefore, we suggest that this LSPR shift decrease is a result of dynamic rearrangement of the CdS during the deposition process. Shown in Figure 3b (dashed pink curve) is a fit aimed at matching the later time LSPR shift. This fit required a CdS fraction of 62.5%. More interestingly, this fit also showed a better match to the early stage data (as compared to the 74%) case, supporting our earlier comment that the CdS fraction likely changes during the deposition process. However, more elaborate morphology studies in the future will be needed to confirm this later time effect.

We performed elemental chemical analysis of the deposited CdS by a combination of EDS and Raman measurements to identify the role of the underlying Ag NPs on film growth. Figure 4g corresponds to the elemental map of Ag and Figure 4h corresponds to that of Cd, both obtained by doing EDS measurements on a 5 min deposited sample. To quantify how much of the CdS deposit overlapped with the position of the Ag NPs, the intensity matrices for the Ag and the Cd maps were obtained by multiplying the two matrices element by element. The correlation plot for the overlapping regions of the two materials is shown in Figure 4c. The coverage of Ag, Cd, and both Ag and Cd were calculated as a percentage of the total number of pixels: 5.86% of the pixels were occupied by Ag only, 6.3% were occupied by Cd, while only 1.1% of the pixels were occupied by both Ag and Cd. This implied that of the total deposited area, only 8% contained both Ag and CdS (as compared to ∼48% for Cd and ∼44% of Ag), and Ag was not a strong influence on the deposition of CdS under dynamic deposition. Further evidence that Ag NPs did not play a significant role on the growth of CdS on quartz can be obtained from the inset in Figure 2b, which shows CdS morphology to be very similar to the one on Ag NP/quartz. In addition, the rate of growth was also not significantly influenced by the presence of Ag, as suggested by the comparable thickness of the films grown on the two substrates after 5 min of deposition, as seen in Figure 2b. Overall, the picture that emerged for the growth of CdS can be summarized as follows. During early stages, CdS deposited nearly randomly onto the underlying Ag NP/quartz substrate, and at later stages it preferentially deposited onto underlying CdS.

Figure 5a shows the Raman spectra from CdS films deposited onto the Ag NP/quartz as well as quartz samples. The spectra was obtained by averaging the Raman signal from five locations over each of the substrates, each having an area of 0.853 μm^2 over the substrates. The primary peak for CdS occurs at 305 cm^{-1},[30] while the second-order scattering of the LO phonons occur at around 600 cm^{-1};[31] the peak at about 466 cm^{-1}[32] corresponds to quartz. From the spectra it was evident that CdS was indeed being deposited. It was also clear that as deposition time increased, the Raman intensity also increased. This is shown in Figure 5b, where the integrated intensity under the primary CdS peak at 305 cm^{-1} as a function of deposition time on the Ag NP/quartz substrate (closed

DOI: 10.1021/jp512738b
J. Phys. Chem. C 2015, 119, 5033−5039

symbols, left y axis) is plotted. Most importantly, like the saturation in the LSPR shift, the Raman intensity also showed a saturation around the same time as the LSPR shift. This is due to the fact that the Raman signal is likely being enhanced due to the plasmonic effect of the Ag NPs.[33] This was further confirmed by other results. In Figure 5b (open symbols, right y axis), it can also be seen that the Raman intensity for the control CdS film deposited for 30 min on pure quartz was significantly lower than the ones for CdS deposited on Ag NPs. From AFM analysis, we determined that the thickness of the film on quartz following 30 min deposition was 207 nm. Despite this large thickness, the intensity of the Raman signal for the CdS/quartz was substantially weaker than most of the CdS/Ag NP/quartz samples. The reason for this was the surface-enhanced Raman scattering (SERS) effect for the CdS regions in close proximity to the Ag NPs.[33] We quantified the SERS enhancement factor as a function of deposition time by using the following equation: $I_{enhanced}/I_{normal}$, where the $I_{enhanced}$ represents the Raman intensity enhanced by the Ag NPs and I_{normal} represents the Raman intensity without the Ag NPs, and both were normalized with respect to CdS film deposition time. Figure 5c shows the plot of the calculated SERS enhancement factor as a function of CdS deposition time (■). As expected from the slowing trend of the total Raman intensity (Figure 5b), the enhancement factor decayed exponentially with increasing deposition time. This enhancement decay with increasing deposition time also correlated well with the LSPR shift observations. Figure 5c also compares the enhancement factor (dashed line) with the rate of change of the LSPR shift with time (solid line). The similarity in the two trends clearly indicates that the Raman scattering enhancement factor from the underlying LSPR substrates can also shed very useful information on the film growth kinetics. Figure 5a also helped clarify that silver sulfide (Ag_2S) was not being formed since its strongest Raman peak at 188 cm^{-1}[34] is missing. This is consistent with the fact that from thermodynamics, the heat of formation of CdS is −161.9 kJ/mol and is much larger than that of Ag_2S, which is −29.4 kJ/mol.[35]

■ CONCLUSIONS

In this paper, we used in situ LSPR spectroscopy to investigate the early stage deposition of CdS via dynamic CBD on a quartz substrate containing Ag nanoparticles. By combining the in situ LSPR measurements with ex situ SEM, EDS, AFM, and Raman measurements, we found that the deposition of CdS begins as a random growth on the underlying substrate but changes to preferred deposition onto existing CdS at later times. These changes in morphology could be interpreted from the LSPR wavelength shift. A strong SERS effect was observed stemming from the configuration of having a semiconductor (CdS) deposited onto Ag NP/quartz substrates, and this enhancement factor correlated well with the LSPR wavelength shift. These results of in situ LSPR and ex situ SERS effects could serve in the future as the basis for an elaborate exploration to understand and control the early stage deposition and growth kinetics of materials from the liquid phase for photovoltaic and battery applications. However, this technique will not be applicable for monitoring the bulk film growth on metallic substrates.

■ EXPERIMENTAL METHODS

Since the goal of this work was to detect changes in the LSPR signal in broadband optical spectra during in situ dynamic flow deposition of CdS, a transparent perspex flow cell was used. The schematic layout of the dynamic measurement technique is shown in Figure 6. The liquid was flowed through the

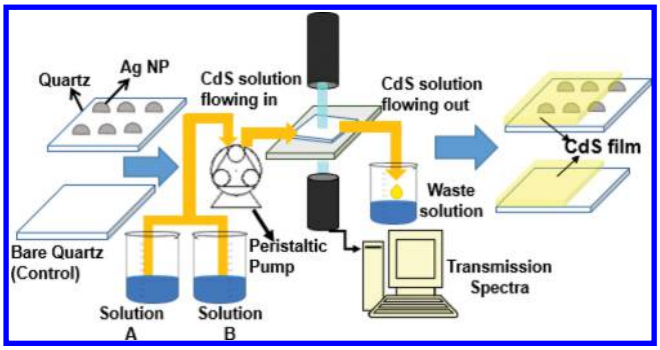

Figure 6. Schematic diagram showing the experimental procedure for in situ measurement of LSPR during CBD deposition.

transparent flow cell, which was placed at normal incidence between one fiber that transmitted the broadband UV−vis light from a DH-2000 (i.e., deuterium and halogen) lamp from Mikropack and a second collection fiber that was coupled to an Ocean Optics HR 2000+ spectrometer. The investigations were performed on two types of transparent quartz substrates. On one, a monomodal distribution of Ag nanoparticles were fabricated by a laser dewetting technique. First, the quartz substrates were sonicated in acetone, iso-propanol, and distilled water, in that order, for 15 min each. Next, Ag films of ∼5 nm thickness were deposited on the dried quartz substrates via e-beam evaporation under ultrahigh vacuum (1×10^{-8} Torr). The films were then irradiated in air by 1000 pulses from a nanosecond pulsed ND:YAG (Quanta Ray, Spectra Physics) laser of wavelength λ = 266 nm with the energy density chosen to be at the melt threshold energy for the Ag film. This resulted in creation of an array of Ag nanoparticles of 32 ± 6 nm average diameter.[36] The other substrate was the bare quartz subjected to the same cleaning conditions mentioned above. The details of the solution used to deposit CdS were as follows.[6] One molar cadmium acetate solution, titrated with ammonium hydroxide, and 1 molar thiourea solution, both having deionized (DI) water as the solvent, were used as precursors for the CdS solution. The precursor solutions were flowed through tubes into a peristaltic pump, which helped mix the two solutions and pump the resulting CdS solution over the substrates at a constant flow rate. The flow rate used in our experiment was 6.36 mL/min. The substrates were masked on the back surface and on an edge using clear nail polish to prevent deposition of CdS on those regions of the substrate while still allowing transmission measurements to be made. Control samples were prepared by depositing CdS films on bare quartz substrates using the same procedure. The optical transmission spectra were typically recorded in 10 s intervals during the dynamic deposition. We also prepared CdS film samples on the Ag NP/quartz substrates for ex situ characterization by stopping the flow following various deposition times of 3, 5, 10, 12, 15, and 20 min at the same flow rate of 6.36 mL/min. Control samples of CdS/quartz were made for 5 and 30 min of deposition times. Once the in situ deposition was complete, the samples were dried in air and their optical

DOI: 10.1021/jp512738b
J. Phys. Chem. C 2015, 119, 5033−5039

transmission spectra were collected. To ensure reproducibility of results, the in situ and ex situ optical measurements were repeated such that each dynamic time had between 2 to 10 independent measurements.

The morphology and elemental analysis of select samples were subsequently characterized by scanning electron microscopy (SEM) and energy dispersive X-ray spectroscopy (EDS) using a Zeiss Merlin SEM. The thickness of the deposited CdS film was determined by performing atomic force microscopy (AFM; Alpha 300 from WITech) measurements of the step height created by masking the samples. AFM measurements were done in intermittent contact mode using silicon AFM probe tips (force constant = 3 N/m, Budget Sensors). Raman spectra on select samples were acquired with an Alpha 300 confocal Raman microscope (WITech, GmbH) using solid-state 532 nm excitation laser and a 20× objective to obtain a spatial map of CdS film on the samples and to compare the intensity of the Raman signals from CdS on Ag NPs against the control samples with CdS on quartz.

AUTHOR INFORMATION

Corresponding Authors

*E-mail: nandaj@ornl.gov.

*E-mail: ramki@utk.edu.

Notes

The authors declare no competing financial interest.

ACKNOWLEDGMENTS

This work was supported by TN-SCORE Grant NSF-EPS-1004083, while A. Malasi was supported by grant ARMY W911NF-13-1-0428. J.N. and R.E.R. acknowledge support from the Laboratory Directed Research and Development Program of Oak Ridge National Laboratory, managed by UT-Battelle, LLC, for the U.S. Department of Energy. R.K. and H.T. also acknowledge CNMS2013-284 at the Center for Nanophase Materials Science, which is sponsored at ORNL by the Scientific User Facilities Division, Office of Basic Energy Sciences, U.S. Department of Energy for SEM characterization.

REFERENCES

(1) Taur, V. S.; Joshi, R. A.; Sharma, R. Annealing-induced modifications in physicochemical and optoelectronic properties of Ag-doped nanostructured CdS thin films. *Int. J. Photoenergy* **2012**, 1–7.

(2) Oliva, A.; Corona, J.; Patino, R.; Oliva-Aviles, A. Chemical bath deposition of CdS thin films doped with Zn and Cu. *Bull. Mater. Sci.* **2014**, *37*, 247–255.

(3) Nair, P.; Nair, M.; Garcia, V.; Arenas, O.; Pena, Y.; Castillo, A.; Ayala, I.; Gomezdaza, O.; Sanchez, A.; Campos, J.; et al. Semiconductor thin films by chemical bath deposition for solar energy related applications. *Sol. Energy Mater. Sol. Cells* **1998**, *52*, 313–344.

(4) Ortega-Borges, R.; Lincot, D. Mechanism of chemical bath deposition of cadmium sulfide thin films in the ammonia-thiourea system. In situ kinetic study and modelization. *J. Electrochem. Soc.* **1993**, *140*, 3464–73.

(5) Tran, T.; Ngo, D. T.; Vu, T. H.; Nguyen, T. D.; Ha, C.-S. Transformation of the structural surface morphology and electronic structure of CdS nanostructured films prepared in glycerol-containing solution, under ultrasonic irradiation. *Adv. Nat. Sci.: Nanosci. Nanotechnol.* **2010**, *1*, 1–4.

(6) Gopal, V. *New Dielectric Coatings for Low-Loss Hollow Glass Waveguides and Bundles.* Ph.D. Thesis, Rutgers University, **2003**.

(7) Tomakin, M.; Oncel, Y.; Keskenler, E. F.; Nevruzoglu, V.; Onuk, Z.; Gorur, O. Investigation of $Cd_{1-x}Co_xS$ diluted magnetic semiconductor thin films fabricated by chemical bath deposition method. *J. Alloys Compd.* **2014**, *616*, 166–172.

(8) Zhang, R.; Liu, J.; Guo, H.; Tong, X. Hierarchically porous nickel oxide nanoflake arrays grown on carbon cloth by chemical bath deposition as superior flexible electrode for supercapacitors. *Mater. Lett.* **2014**, *136*, 198–201.

(9) Mu, W. N.; Shi, S. Z. Fabrication and Characterization of TiO_2-Organic Thin Film From an Aqueous Solution. *Polym. Polym. Compos.* **2014**, *22*, 699–704.

(10) Roy, P.; Ota, J. R.; Srivastava, S. K. Crystalline ZnS thin films by chemical bath deposition method and its characterization. *Thin Solid Films* **2006**, *515*, 1912–1917.

(11) Dhyani, H.; Srivastava, S.; Ali, M. A.; Malhotra, B. D.; Sen, P. Fabrication of nanocrystalline CdS electrode via chemical bath deposition technique for application to cholesterol sensor. *J. Phys.: Conf. Ser.* **2012**, *358*, 012008.

(12) Hodes, G. Semiconductor and ceramic nanoparticle films deposited by chemical bath deposition. *Phys. Chem. Chem. Phys.* **2007**, *9*, 2181–2196.

(13) Iwashita, T.; Ando, S. Preparation and characterization of ZnS thin films by the chemical bath deposition method. *Thin Solid Films* **2012**, *520*, 7076–7082.

(14) Saez-Araoz, R.; Abou-Ras, D.; Niesen, T.; Neisser, A.; Wilchelmi, K.; Lux-Steiner, M.; Ennaoui, A. In situ monitoring the growth of thin-film ZnS/Zn(S,O) bilayer on Cu-chalcopyrite for high performance thin film solar cells. *Thin Solid Films* **2009**, *517*, 2300–2304.

(15) Wakeling, B.; Degamber, B.; Kister, G.; Lane, D.; Bailey, M.; Jeynes, C. In situ analysis of cadmium sulphide chemical bath deposition by an optical fibre monitor. *Thin Solid Films* **2012**, *525*, 1–5.

(16) Greil, S. M.; Lauermann, I.; Ennaoui, A.; Kropp, T.; Lange, K. M.; Weber, M.; Aziz, E. F. In situ investigation of wet chemical processes for chalcopyrite solar cells by L-edge XAS under ambient conditions. *Nucl. Instrum. Methods Phys. Res., Sect. B* **2010**, *268*, 263–267.

(17) Jang, G. G.; Blake, P.; Roper, D. K. Rate-limited electroless gold thin film growth: A real-time study. *Langmuir* **2013**, *29*, 5476–5486. PMID:23560793

(18) Jain, P. K.; Huang, X.; El-Sayed, I. H.; El-Sayed, M. A. Noble metals on the nanoscale: Optical and Photothermal properties and some applications in imaging, sensing, biology, and medicine. *Acc. Chem. Res.* **2008**, *41*, 1578–1586.

(19) Willets, K. A.; van Duyne, R. P. Localized surface plasmon resonance spectroscopy and sensing. *Annu. Rev. Phys. Chem.* **2007**, *58*, 267–297.

(20) Liao, H.; Nehl, C. L.; Hafner, J. H. Biomedical applications of plasmon resonant metal nanoparticles. *Nanomedicine* **2006**, *1*, 201–208.

(21) Frolov, L.; Dix, A.; Tor, Y.; Tesler, A. B.; Chaikin, Y.; Vaskevich, A.; Rubinstein, I. Direct observation of aminoglycoside RNA binding by localized surface plasmon resonance spectroscopy. *Anal. Chem.* **2013**, *85*, 2200–2207.

(22) Teichroeb, J. H.; Forrest, J. A.; Ngai, V.; Jones, L. W. Anomalous thermal denaturing of proteins adsorbed to nanoparticles. *Eur. Phys. J. E: Soft Matter Biol. Phys.* **2006**, *21*, 19–24.

(23) Stuart, D. A.; Haes, A. J.; Yonzon, C. R.; Hicks, E. M.; van Duyne, R. P. Biological applications of localised surface plasmonic phenomenae. *IEE Proc.: Nanobiotechnol.* **2005**, *152*, 13–32.

(24) Sapra, S.; Nanda, J.; Sarma, D.; El-Al, F. A.; Hodes, G. Blue emission from cysteine ester passivated cadmium sulfide nanoclusters. *Chem. Commun. (Cambridge, U. K.)* **2001**, 2188–2189.

(25) Kamat, P. V. Quantum Dot Solar Cells. Semiconductor nanocrystals as light harvesters. *J. Phys. Chem. C* **2008**, *112*, 18737–18753.

(26) Park, W.-D. Optical constants and dispersion parameters of CdS thin film prepared by chemical bath deposition. *Transactions on Electrical and Electronic Materials* **2012**, *13*, 196–199.

DOI: 10.1021/jp512738b
J. Phys. Chem. C 2015, 119, 5033–5039

(27) Garcia, H.; Trice, J.; Kalyanaraman, R.; Sureshkumar, R. Self consistent determination of plasmonic resonance in ternary nanocomposites. *Phys. Rev. B* **2007**, *75*, 045439−1−4.
(28) Garcia, H.; Sachan, R.; Kalyanaraman, R. Optical plasmon properties of Co-Ag nanocomposites within the mean-field approximation. *Plasmonics* **2012**, *7*, 137−141.
(29) Singh Sekhon, J.; Verma, S. Refractive index sensitivity analysis of Ag, Au, and Cu nanoparticles. *Plasmonics* **2011**, *6*, 311−317.
(30) Oladeji, I. O.; Chow, L.; Liu, J. R.; Chu, W. K.; Bustamante, A. N. Comparative study of CdS thin films deposited by single, continuous, and multiple dip chemical processes. *Thin Solid FIlms* **2000**, *359*, 154−159.
(31) Myung, N. V., Tao, N., Podlaha-Murphy, E. J., Zangari, G., Mallett, J., Talbot, J., Eds. *Electrodeposition of Nanoengineered Materials and Alloys 2*; The Electrochemical Society: Pennington, NJ, 2008; Vol. *11*.
(32) Gillet, P.; le Cleac'h, A.; Madon, M. High-temperature raman spectroscopy of SiO_2 and GeO_2 Polymorphs: Anharmonicity and thermodynamic properties at high-temperatures. *J. Geophys. Res.: Solid Earth* **1990**, *95*, 21635−21655.
(33) Fan, M.; Brolo, A. G. Silver nanoparticles self assembly as SERS substrates with near single molecule detection limit. *Phys. Chem. Chem. Phys.* **2009**, *11*, 7381−7389.
(34) Martina, I.; Wiesinger, R.; Jembrih-Simbürger, D.; Schreiner, M. Micro-Raman characterization of silver corrosion products: Instrumental set up and reference database. *e-Preserv. Sci.* **2012**, *9*, 1−8.
(35) Inorganic Compounds: Physical and Thermochemical Data. http://www2.ucdsb.on.ca/tiss/stretton/database/inorganic_thermo.htm (accessed January 23, 2015).
(36) Krishna, H.; Sachan, R.; Strader, J.; Favazza, C.; Khenner, M.; Kalyanaraman, R. Thickness-dependent spontaneous dewetting morphology of ultrathin Ag films. *Nanotechnology* **2010**, *21*, 155601.

DOI: 10.1021/jp512738b
J. Phys. Chem. C 2015, 119, 5033−5039